# LETTER

Crystallization of silicon dioxide and compositional evolution of the Earth's core

Kei Hirose[1], Guillaume Morard[2], Ryosuke Sinmyo[1], Koichio Umemoto[1], John Hernlund[1], George Helffrich[1] & Stéphane Labrosse[3]

The Earth's core is about ten per cent less dense than pure iron (Fe), suggesting that it contains light elements as well as iron. Modelling of core formation at high pressure (around 40–60 gigapascals) and high temperature (about 3,500 kelvin) in a deep magma ocean[1–5] predicts that both silicon (Si) and oxygen (O) are among the impurities in the liquid outer core[6–9]. However, only the binary systems Fe–Si and Fe–O have been studied in detail at high pressures, and little is known about the compositional evolution of the Fe–Si–O ternary alloy under core conditions. Here we performed melting experiments on liquid Fe–Si–O alloy at core pressures in a laser-heated diamond-anvil cell. Our results demonstrate that the liquidus field of silicon dioxide (SiO$_2$) is unexpectedly wide at the iron-rich portion of the Fe–Si–O ternary, such that an initial Fe–Si–O core crystallizes SiO$_2$ as it cools. If crystallization proceeds on top of the core, the buoyancy released should have been more than sufficient to power core convection and a dynamo, in spite of high thermal conductivity[10,11], from as early on as the Hadean eon[12]. SiO$_2$ saturation also sets limits on silicon and oxygen concentrations in the present-day outer core.

Recent core-formation models propose that the present outer core contains 2 wt% Si and 5 wt% O by assuming relatively oxidizing conditions[4], or 8–9 wt% Si and 2–4 wt% O by assuming relatively reducing conditions[8,9]. We examined the fate of a cooling liquid Fe–Si–O alloy spanning a similar range of compositions starting with four distinct compositions in seven runs (Table 1) using a combination of high-pressure, high-temperature experiments in a laser-heated diamond-anvil cell (DAC) and textural/chemical characterizations of recovered samples. Beginning with an ultrafine-grained homogeneous mixture (Extended Data Fig. 1), after several seconds of heating we obtained a pool of quenched molten iron alloy in contact with solid SiO$_2$ at the outer (colder) portion in all runs (Fig. 1 and Extended Data Fig. 2). Owing to an intrinsic temperature gradient in the DAC, both melting and crystallization occurred simultaneously in the laser-heated sample, melting in its hotter portion and

crystallization in its colder portion. Disequilibrium caused by the Soret effect is often observed in high-temperature experiments on silicates[13], and typically enriches silicon and iron in hot and cold regions, respectively. Instead, our present observations show the opposite distribution, while the homogeneity of the melted portion—as expected from the fast diffusion of Si and O in liquid Fe (ref. 14)—and its physical contact with the solid SiO$_2$ imply that conditions were not far from equilibrium (see Methods). From these observations, we infer that solid SiO$_2$ crystallizes from an Fe–Si–O ternary alloy, and
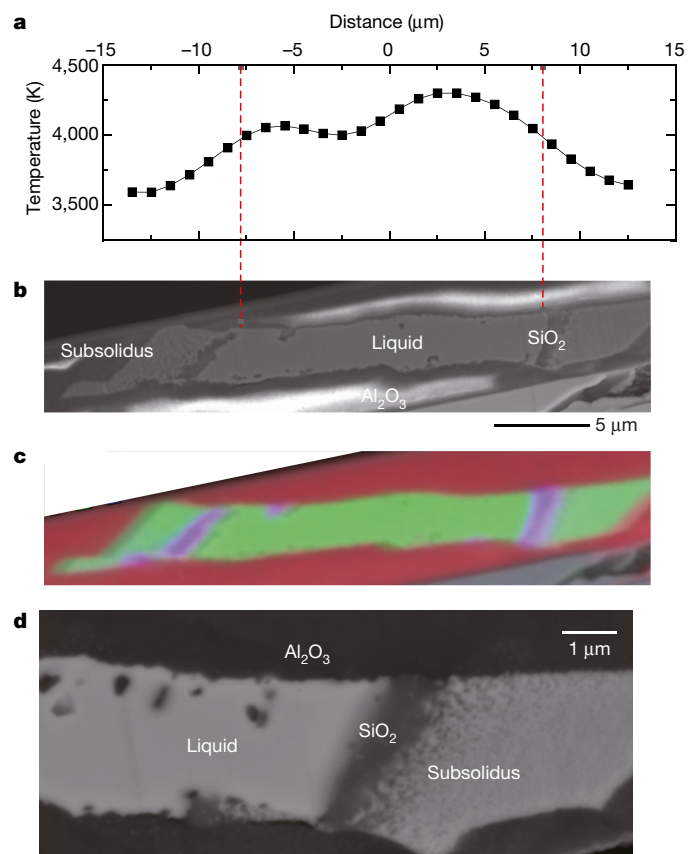
Figure 1 | Melting experiment (run 1) at 142 GPa. a, Radial temperature distribution on the sample surface. b, Secondary electron image of the sample's cross-section. c, Composite X-ray map showing quenched (Si + O)-depleted Fe liquid (green) at the centre, surrounded by solid SiO$_2$ (purple) and surrounding unmelted starting material (green). Samples were sandwiched between Al$_2$O$_3$ insulation layers (red). d, Back-scattered electron image of quenched liquid alloy, solid SiO$_2$, and subsolidus material. The homogeneity of the metallic part is consistent with a quench texture from the molten state.

Table 1 | Results of melting experiments

Run number	Starting material		Pressure (GPa)	Temperature (K)	Liquid Fe	
	Si (wt%)	O (wt%)			Si (wt%)	O (wt%)
1	3.8 ± 0.2	4.4 ± 0.2	142	3,990	0.6 ± 0.1	1.3 ± 0.2
2	4.9 ± 0.1	5.6 ± 0.2	52	2,910	0.6 ± 0.0	0.8 ± 0.0
3	12.1 ± 0.3	8.3 ± 0.5	63	3,050*	6.7 ± 0.1	0.1 ± 0.2
4	12.1 ± 0.3	8.3 ± 0.5	133	3,920	5.8 ± 0.1	0.5 ± 0.0
5	12.1 ± 0.3	8.3 ± 0.5	194	4,560	4.5 ± 0.6	0.7 ± 0.2
6	9.7 ± 0.5	13.4 ± 1.4	145	3,860†	1.1	3.7
7	9.7 ± 0.5	13.4 ± 1.4	141	3,860	0.4 ± 0.3	4.4 ± 0.8

*Estimated from the liquidus temperature of Fe–7 wt% Si (ref. 30).
†Assumed to be the same as in run 7.
Errors correspond to 1σ. The uncertainties in pressure and temperature may be ±10% and ±3%, respectively.

[1]Earth-Life Science Institute, Tokyo Institute of Technology, 2-12-1 Ookayama, Meguro, Tokyo 152-8550, Japan. [2]Institut de Minéralogie, de Physique des Matériaux et de Cosmochimie, UMR CNRS 7590, Sorbonne Universités—Université Pierre et Marie Curie, CNRS, Muséum National d'Histoire Naturelle, IRD, 4 Place Jussieu, 75005 Paris, France. [3]Université de Lyon, École normale supérieure de Lyon, Université Lyon-1, CNRS, UMR 5276 LGL-TPE, F-69364 Lyon, France.

in the Earth's core this may be a gradual process coupled to secular cooling that exerts an important influence on core composition, dynamics and the geodynamo.

Four of our experiments, with three different starting compositions, were performed at uppermost-core pressures (133–145 GPa) and temperatures of about 4,000 K (Table 1). The composition of molten iron found in run 1 was Fe–0.6 wt% Si–1.3 wt% O (starting composition Fe–3.8 wt% Si–4.4 wt% O), indicating that liquid Fe–Si–O alloy crystallized SiO$_2$ oxide until most of the silicon and oxygen were consumed from the liquid. The temperature at the liquid/solid boundary was estimated to be 3,990 ± 120 K at 142 GPa (Fig. 1a), close to the melting temperature of pure iron[15]. In run 4, we obtained liquid Fe–5.8 wt% Si–0.5 wt% O from silicon-rich Fe–Si–O starting material, showing that silicon-rich liquid Fe–Si–O crystallized SiO$_2$ oxide until the supply of oxygen in the metallic melt was exhausted. Similarly in run 7, oxygen-rich Fe–Si–O liquid evolved to nearly silicon-free liquid Fe–0.4 wt % Si–4.4 wt % O via crystallization of SiO$_2$. These results are consistent with crystallization of SiO$_2$ from an Fe–Si–O metallic liquid until one (or both) of silicon and oxygen is (are) nearly depleted.

The liquidus field of SiO$_2$ (the compositional range in which SiO$_2$ crystallizes first) occupies a large portion of the Fe–Si–O ternary system at uppermost core pressures (Fig. 2a). This is consistent with the phase diagram in the FeO–SiO$_2$ binary system, which exhibits a eutectic very close to the FeO endmember (>99.4 wt% FeO)[16]. These results are also consistent with earlier reports[5,7,9] on metal–silicate partitioning of Si and O (Extended Data Figs 3 and 4). Using these data, we developed a thermodynamical model of SiO$_2$ saturation in liquid Fe (Fig. 2b). Depending on predictions for the original core composition[4,8,9], SiO$_2$ crystallization near core–mantle boundary (CMB) pressure would begin after cooling to 4,500–5,200 K (note that the temperature of core metal increases during descent, for example from 3,400 K at 54 GPa to 4,725–5,724 K at 135 GPa with 10%–25% gravitational potential energy release). Thus, if the present-day CMB temperature is at 4,000 K, the current outer core has been subjected to SiO$_2$ crystallization and is likely to be depleted in either Si (<0.7 wt%) or O (<1.0 wt%). Both Si and O could be depleted if the initial core had a molar ratio of Si:O close to 1:2 (that is, stoichiometric SiO$_2$).

The present results impose new constraints upon the composition of the Earth's core. In particular, the outer core cannot include both Si and O at concentrations higher than is permitted by SiO$_2$ saturation. Recent calculations by ref. 17 argued that the density and seismic velocity of the outer core are best explained by liquid Fe–1.9 wt% Si–3.7 wt% O, but this is ruled out by our experiments unless the CMB temperature is higher than 4,400 K (Fig. 2b). In addition, the Si-rich initial core compositions proposed by refs 8 and 9 are unlikely to be consistent with inner-core properties because they evolve to the Si-rich side of the Fe–FeSi eutectic via the crystallization of SiO$_2$ and then form CsCl-type Fe–Si alloy[18].

Because our experiments were conducted at shallow core conditions, our uncertainties are too large to constrain whether SiO$_2$ saturation increases or decreases along adiabats at pressures deep inside the core (Extended Data Fig. 5). Thus we cannot reliably predict whether SiO$_2$ crystallization from an initially well-mixed isentropic liquid Fe–Si–O core would begin from the top or the centre. The slopes of adiabatic saturation curves suggest that crystallization from the centre might be preferred. Equilibrium crystallization of SiO$_2$ driven by secular cooling that begins from the centre would produce an outwardly expanding (Si + O)-depleted region, as buoyant SiO$_2$ is expelled to shallower depths where it may dissolve into under-saturated fluid. However, if the residual liquid follows SiO$_2$ saturation, then it will be progressively more depleted in Si + O (and hence more dense) with increasing depth. Unless this residual gravitationally stable density stratification were to be mixed away (for which there is at present no proposed mechanism), the advance of the SiO$_2$ crystallization front to the CMB would produce an outer core that is not well mixed and isentropic, contrary to geomagnetic and seismic inferences.
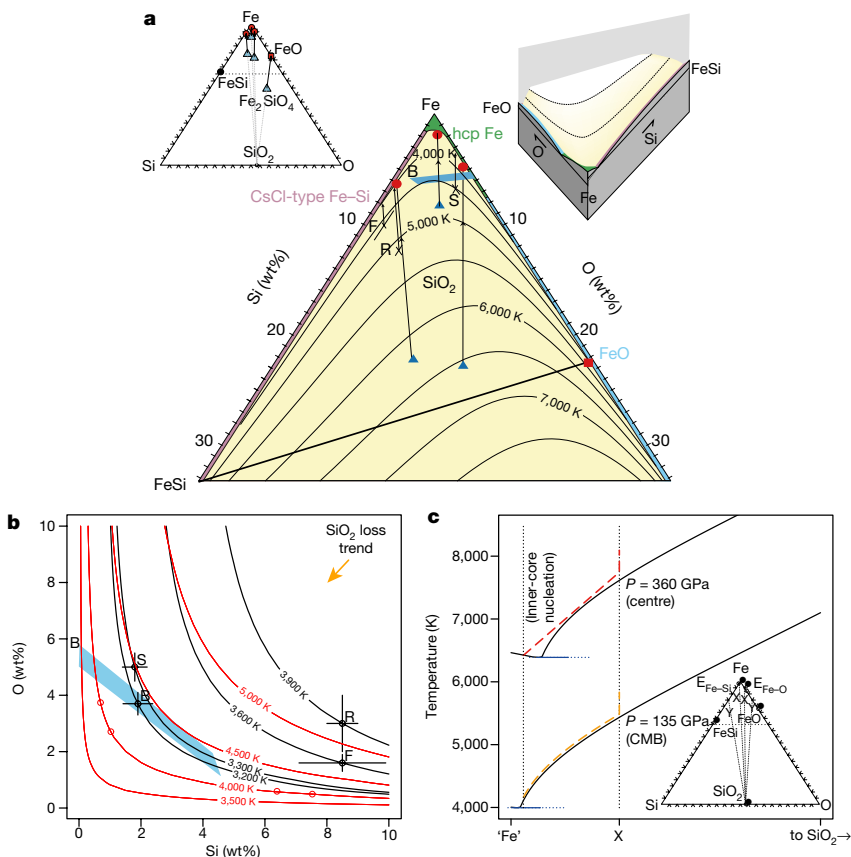
Figure 2 | Crystallization of SiO$_2$ from liquid Fe–Si–O. **a**, Liquidus phase relations in Fe–Si–O at about 135 GPa. The right inset illustrates the topology with temperature as the vertical axis. Our data are shown as red circles (liquid compositions) and blue triangles (their starting materials). The eutectic composition in the FeO–SiO$_2$ join is indicated by a red square[16]. Note the large compositional range (yellow) in which SiO$_2$ crystallizes first. Arrows show liquid compositions evolving away from SiO$_2$ upon crystallization in the yellow region (see the entire ternary diagram, left inset). Metal crystallization starts after the liquid becomes depleted in either Si or O. Green, pink and blue areas are the liquidus fields of hexagonal close-packed (hcp) Fe, CsCl-type Fe–Si and FeO, respectively[18,27]. **b**, Solubility limits for SiO$_2$ in core metal according to our model at 54 GPa (the typical core–mantle separation pressure[9], black) and 135 GPa (the SiO$_2$ crystallization pressure, red). The compositions marked 'S', 'R' and 'F' in **a** and **b** show original core compositions[4,8,9] with uncertainties given by error bars. Those labelled 'B' indicate the possible range (blue region) and the best estimate (circle with error bars) of the present-day outer-core composition[17]. Circles on the T_{CMB} = 4,000 K contour show the current Si and O contents in the outer core starting from these compositions. **c**, Schematic illustration of secular core cooling at the CMB (yellow) and the centre (red) until inner-core nucleation. The liquid core composition changes from its original 'X' (see inset) as the core cools and crystallizes SiO$_2$ at the CMB, losing Si + O to the mantle. This shift in core composition to the Fe-rich side of the eutectic 'E$_{Fe–Si}$' or 'E$_{Fe–O}$' eventually induces Fe-rich metal crystallization at the centre. Compositions 'Y' do not ultimately crystallize Fe, but rather FeO or Fe–Si.
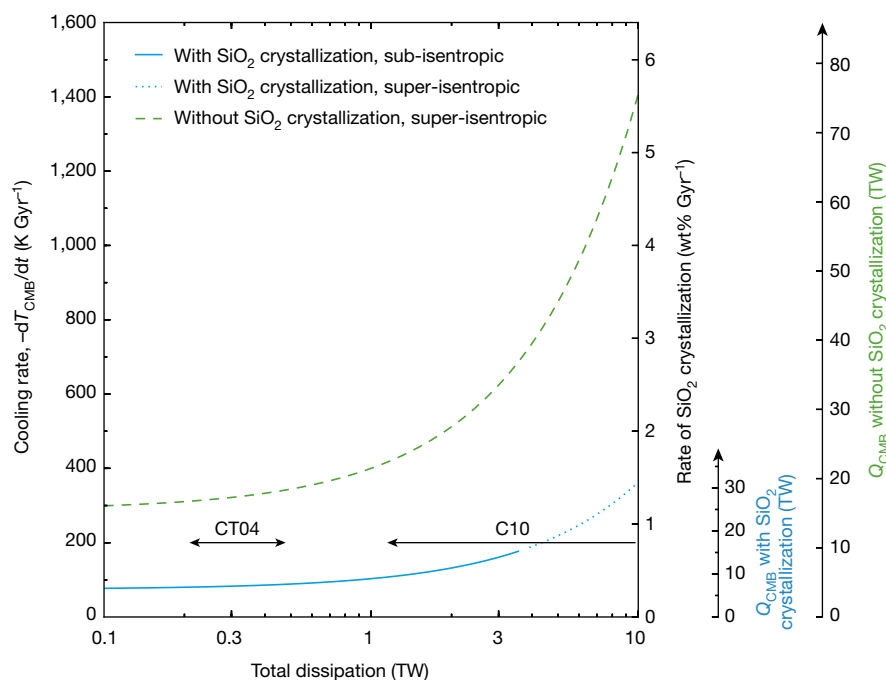
Figure 3 | Core cooling rate with SiO₂ crystallization. The cooling rate, crystallization rate and the CMB heat flow (Q_{CMB}; with and without SiO₂ crystallization) necessary to sustain the geodynamo are plotted as a function of assumed total dissipation for the time just preceding the onset of inner-core crystallization (see Methods). The blue (dashed green) curve gives the value obtained by taking (without taking) into account the compositional buoyancy provided by crystallizing SiO₂ at the CMB, with the corresponding CMB heat flows given on the right-hand scales. The blue line is dotted where the CMB heat flow is larger than the isentropic value (13.8 TW). The horizontal arrows give the ranges of ohmic dissipation in the present core proposed by ref. 28 (CT04) and ref. 29 (C10) using scaling laws obtained from geodynamo models, all running in a super-isentropic heat flow regime.

Our data and model also permits an alternative scenario in which crystallization proceeds at shallower depths first, with buoyant SiO₂ accumulating on the top of the core and producing a denser $(Si + O)$-depleted liquid that would sink into the deeper core, thus helping to drive core convection. In this scenario, SiO₂ crystallization would continue today at the CMB, while the progressively $(Si + O)$-depleted outer-core liquid would crystallize solid Fe-rich metal at the inner-core boundary (Fig. 2c). The previously accepted scenario of the convectively driven geodynamo as the origin of the magnetic field of the Earth has been recently challenged by (1) the upward revision of the thermal conductivity of the core, which implies an inner-core nucleation younger than 1.4 billion years (Gyr) and (2) a total secular cooling of the core in excess of 1,000 K (ref. 19) to drive thermal convection before 1.4 Gyr ago, which is required to explain palaeomagnetic intensity measurements[12]. However, before the growth of the inner core (which provides a compositional buoyancy source to drive core convection at present), we estimate that crystallization of SiO₂ on top of the core allows for a secular core cooling rate 3.88 times smaller than is required for unassisted thermal convection alone[19] (Fig. 3), and the requisite CMB heat flow to sustain the dynamo is 2.75 times smaller (Fig. 3). Even if we assume a relatively high core thermal conductivity (exceeding $90\ W\ m^{-1}\ K^{-1}$), as proposed in recent studies[10], a geodynamo with ohmic dissipation of 1 TW could be maintained by core convection while crystallizing SiO₂ and cooling at a modest rate of about 100 K Gyr⁻¹.

Using our thermodynamical model, we estimate that secular core cooling of around 100 K at saturation would crystallize about 0.4 wt% SiO₂ (Fig. 2b; see Methods) to produce a pure layer of SiO₂ that is about 2 km thick at the CMB. The fate of this SiO₂ depends on the nature of the base of the mantle. If the mantle were extensively molten[20], then SiO₂ cumulates would react with the magma and promote crystallization of $(Mg,Fe)SiO_3$-bridgmanite, because it is the expected liquidus phase over a wide range of pressures and melt compositions in the deep mantle[21]. If there is no basal melt and SiO₂ underplates the base of a solid mantle, it could initially form a dense mush containing liquid iron in the solid interstices, similar to a previously proposed scenario[22]. Such a mixture would undergo viscous compaction as the liquid is expelled and may form a high electrical conductivity layer at the CMB if it retains sufficient interstitial metal to form an interconnected network[22]. In this latter case, the SiO₂ mushy cumulates would be subjected to viscous coupling with solid basal mantle flows, and swept towards convergent upwelling zones, possibly consistent with seismically observed ultralow-velocity zones, depending on the thickness and residual iron liquid fraction[23].

Our experiments show that one need not invoke singular events to resolve the enigma of powering a long-running dynamo[12]. Rather than requiring core formation at extremely high temperatures (exceeding 5,000 K) to introduce a certain amount of Mg into the core[24,25], sufficient $Si + O$ can be incorporated via the metal-segregation processes in a deep magma ocean at moderate temperatures[1–5,7–9]. Thus the model is potentially as applicable to dynamos operating in asteroidal bodies[26] as to the dynamos operating in the Earth.

Online Content Methods, along with any additional Extended Data display items and Source Data, are available in the online version of the paper; references unique to these sections appear only in the online paper.

1. Wood, B. J., Walter, M. J. & Wade, J. Accretion of the Earth and segregation of its core. *Nature* **441,** 825–833 (2006).
2. Rubie, D. *et al.* Heterogeneous accretion, composition and core–mantle differentiation of the Earth. *Earth Planet. Sci. Lett.* **301,** 31–42 (2011).
3. Righter, K. Prediction of metal–silicate partition coefficients for siderophile elements: an update and assessment of PT conditions for metal–silicate equilibrium during accretion of the Earth. *Earth Planet. Sci. Lett.* **304,** 158–167 (2011).
4. Siebert, J., Badro, J., Antonangeli, D. & Ryerson, F. J. Terrestrial accretion under oxidizing conditions. *Science* **339,** 1194–1197 (2013).
5. Bouhifd, M. A. & Jephcoat, A. P. Convergence of Ni and Co metal–silicate partition coefficients in the deep magma-ocean and coupled silicon–oxygen solubility in iron melts at high pressures. *Earth Planet. Sci. Lett.* **307,** 341–348 (2011).

6. Takafuji, N., Hirose, K., Mitome, M. & Bando, Y. Solubilities of O and Si in liquid iron in equilibrium with (Mg,Fe)SiO$_3$ perovskite and the light elements in the core. *Geophys. Res. Lett.* **32,** L06313 (2005).
7. Siebert, J., Badro, J., Antonangeli, D. & Ryerson, F. J. Metal–silicate partitioning of Ni and Co in a deep magma ocean. *Earth Planet. Sci. Lett.* **321–322,** 189–197 (2012).
8. Rubie, D. C. *et al.* Accretion and differentiation of the terrestrial planets with implications for the compositions of early-formed Solar System bodies and accretion of water. *Icarus* **248,** 89–108 (2015).
9. Fischer, R. A. *et al.* High pressure metal–silicate partitioning of Ni, Co, V, Cr, Si, and O. *Geochim. Cosmochim. Acta* **167,** 177–194 (2015).
10. Ohta, K., Kuwayama, Y., Hirose, K., Shimizu, K. & Ohishi, Y. Experimental determination of the electrical resistivity of iron at Earth's core conditions. *Nature* **534,** 95–98 (2016).
11. Konôpková, Z. *et al.* Direct measurement of thermal conductivity in solid iron at planetary core conditions. *Nature* **534,** 99–101 (2016).
12. Tarduno, J. A., Cottrell, R. D., Davis, W. J., Nimmo, F. & Bono, R. K. A Hadean to Paleoarchean geodynamo recorded by single zircon crystals. *Science* **349,** 521–524 (2015).
13. Sinmyo, R. & Hirose, K. The Soret diffusion in laser-heated diamond anvil cell. *Phys. Earth Planet. Inter.* **180,** 172–178 (2010).
14. Helffrich, G. Outer core compositional layering and constraints on core liquid transport properties. *Earth Planet. Sci. Lett.* **391,** 256–262 (2014).
15. Anzellini, S., Dewaele, A., Mezouar, M., Loubeyre, P. & Morard, G. Melting of iron at Earth's inner core boundary based on fast x-ray diffraction. *Science* **340,** 464–466 (2013).
16. Kato, C. *et al.* Melting in the FeO–SiO$_2$ system to deep lower-mantle pressures: implications for subducted Banded Iron Formations. *Earth Planet. Sci. Lett.* **440,** 56–61 (2016).
17. Badro, J., Côté, A. S. & Brodholt, J. P. A seismologically consistent compositional model of Earth's core. *Proc. Natl Acad. Sci. USA* **111,** 7542–7545 (2014).
18. Ozawa, H., Hirose, K., Yonemitsu, K. & Ohishi, Y. High-pressure melting experiments on Fe–Si alloys and implications for silicon as a light element in the core. *Earth Planet. Sci. Lett.* **456,** 47–54 (2016).
19. Labrosse, S. Thermal evolution of the core with a high thermal conductivity. *Phys. Earth Planet. Inter.* **247,** 36–55 (2015).
20. Labrosse, S., Hernlund, J. W. & Coltice, N. A crystallizing dense magma ocean at the base of the Earth's mantle. *Nature* **450,** 866–869 (2007).
21. Boukaré, C., Ricard, Y. & Fiquet, G. Thermodynamics of the MgO–FeO–SiO$_2$ system up to 140 GPa: application to the crystallization of Earth's magma ocean. *J. Geophys. Res. Solid Earth* **120,** 6085–6101 (2015).
22. Buffett, B. A., Garnero, E. J. & Jeanloz, R. Sediments at the top of Earth's core. *Science* **290,** 1338–1342 (2000).
23. Hernlund, J. W. & Tackley, P. J. Some dynamical consequences of partial melting in Earth's deep mantle. *Phys. Earth Planet. Inter.* **162,** 149–163 (2007).
24. O'Rourke, J. G. & Stevenson, D. J. Powering Earth's dynamo with magnesium precipitation from the core. *Nature* **529,** 387–389 (2016).
25. Badro, J., Siebert, J. & Nimmo, F. An early geodynamo driven by exsolution of mantle components from Earth's core. *Nature* **536,** 326–328 (2016).
26. Fu, R. R. *et al.* An ancient core dynamo in asteroid Vesta. *Science* **338,** 238–241 (2012).
27. Komabayashi, T. Thermodynamics of melting relations in the system Fe–FeO at high pressure: implications for oxygen in the Earth's core. *J. Geophys. Res. Solid Earth* **119,** (2014).
28. Christensen, U. R. & Tilgner, A. Power requirement of the geodynamo from ohmic losses in numerical and laboratory dynamos. *Nature* **429,** 169–171 (2004).
29. Christensen, U. R. Dynamo scaling laws and applications to the planets. *Space Sci. Rev.* **152,** 565–590 (2010).
30. Fischer, R. A. *et al.* Phase relations in the Fe–FeSi system at high pressures and temperatures. *Earth Planet. Sci. Lett.* **373,** 54–64 (2013).

METHODS

High-pressure, high-temperature experiments. High-pressure, high-temperature conditions were generated in a laser-heated DAC with 90-μm, 120-μm and 300-μm culet diamond anvils. The Fe–Si–O starting materials with four different compositions were made by Fe–Si alloys sputtering on a glass slide under O_2 flow (from Dephis). This technique yields sample homogeneity on the sub-5-nm scale (Extended Data Fig. 1), even for Fe–Si–O compositions that are within a liquid immiscibility gap at room pressure. The Fe–Si–O coating of thickness 5–8 μm was obtained by magnetron cathodic sputtering in reactive mode under vacuum at a pressure of 10^{-6} mbar. Iron atoms are ejected from a target (the cathode) made of an Fe–Si alloy, under the bombardment of the Ar^+ ions. The synthesis of the Fe–Si–O alloy is produced by the reaction between an oxygen gas and the sputtered Fe and Si atoms. For this, oxygen is added to an argon plasma at a constant flow rate. Stoichiometry is controlled by adjusting the oxygen flux and the power applied to the target. During this process, the Fe–Si–O alloy is naturally sputtered onto a glass slide. The chemical composition and homogeneity of the alloy has been measured using a field-emission-type electron microprobe (FE-EPMA, JEOL JXA-8530F) (Table 1). The sample was loaded, together with a pressure medium of Al_2O_3 (except for run 2 using KCl, and run 3 using NaCl), into a hole drilled on a pre-indented Re gasket. After loading, the whole DAC was dried in a vacuum oven at 423 K for >14 h. We then compressed the sample in Ar atmosphere. Contamination of the iron by aluminium was not observed in this study.

After compression to the desired high pressure, the sample was heated from both sides by a couple of 100-W single-mode Yb fibre lasers. We used beam-shaping optics, which converts a Gaussian beam to one with a flat energy distribution and thus reduces the radial temperature gradient in the sample. The laser-heated spot was about 20 μm across. One-dimensional temperature distributions on the surface of the sample were obtained using the spectro-radiometric method. Heating duration was limited to about 3–5 s in order to avoid fluctuations in temperature that would otherwise cause complex melting textures. We estimated temperature at the boundary between the liquid and solid from the measured radial temperature distribution (Fig. 1a and Extended Data Fig. 2). The uncertainty in temperature determination may be ±3%. Pressures were measured at room temperature after heating based on the Raman shift of the culet of a diamond anvil[31]: 110 GPa, 45 GPa, 56 GPa, 101 GPa, 157 GPa, 114 GPa and 110 GPa in runs 1 to 7, respectively. They were then corrected for the contribution of thermal pressure. According to ref. 32, when purely isochoric heating is made, the thermal pressure is written as $\Delta P = \alpha K_T T$, in which α is the thermal expansivity and K_T is the isothermal bulk modulus. The αK_T value is estimated to be about 9 MPa K^{-1} for liquid iron[33] at CMB pressure (136 GPa) and 4,000 K. In this case, 90% of the theoretical thermal pressure value contributes to experimental pressure increase[32]. For runs 2 and 3 performed at low pressures, the lower αK_T value of 4 MPa K^{-1} and 60% of the theoretical value were applied[34]. The overall errors in pressure should be less than ±10% in the present experiments.

Sample analyses. After heating at high pressure, samples were decompressed and recovered from the DAC for textural and chemical characterizations. Cross-sections of the laser-heated portion of the sample were obtained parallel to the compression axis by using a focused Ga ion beam (FEI Versa 3D DualBeam). X-ray maps for Fe, Si, O, and Al were obtained by an energy-dispersive X-ray analyser with an accelerating voltage of 10 kV attached to a field-emission-type scanning electron microscope in the dual beam system (Fig. 1c and Extended Data Fig. 2). The sample cross-section was then examined by an FE-EPMA for quantitative chemical analyses. We employed an acceleration voltage of 10 kV and beam current of 12 nA.

Melting textures. In all of the present experiments, we found (Si + O)-depleted iron alloys at the centre (hot area) with homogeneous chemical compositions. They usually included Al_2O_3 blocks (Extended Data Fig. 2), although not contaminated by aluminium, indicating that they were molten at high temperature. The quenched liquid alloy, showing homogeneous texture, was surrounded by a SiO_2 layer, while unmelted starting material was present outside the SiO_2 layer (cold part). This zoning corresponds to the expected temperature gradient in the laser-heated sample (Fig. 1a and Extended Data Fig. 2).

Although some temperature variation existed within the liquid portion of the sample, the chemical composition of the liquid was homogeneous. Indeed, the diffusion of Si and O in liquid iron is fast enough to have erased any possible chemical gradient due to the Soret effect. Considering the relation $l^2/D = t$ with l the sample width (10 μm) and D the diffusivity (10^{-9} m^2 s^{-1}) (ref. 14), we found an equilibration time of $t = 0.1$ s. The present experiments were longer than this, a few to several seconds. The solid phase stays in contact with the liquid phase (Fig. 1) and melting/crystallization occurs instantaneously. These ensure chemical equilibrium between the liquid pool and solid SiO_2 during heating. Temperatures at the boundary between the liquid alloy and the SiO_2 layer were determined as experimental temperatures based on one-dimensional temperature profiles (Fig. 1a and Extended Data Fig. 2).

Thermodynamic model of SiO_2 saturation temperature. The solubility of SiO_2 in liquid Fe is governed by the reaction

$$SiO_2^{sil} = Si^{met} + 2O^{met} \tag{1}$$

where superscripts 'sil' and 'met' indicate silicate and metal, respectively, whose mutual solubility is governed by an Si–O equilibrium constant K_{Si-O} that reads

$$K_{Si-O} = \frac{a_{Si}^{met}(a_O^{met})^2}{a_{SiO_2}^{sil}} \tag{2}$$

The Si and O solubilities in liquid Fe are inversely related and depend principally on temperature[35], indicating that, approximately, $X_{Si}^{met} X_O^{met} = f(T)$, where $f(T)$ is some function of temperature. Extended Data Fig. 3 shows the experimental data on Si and O solubility. The unmodelled X_{Si} and X_O data shows that $\log_{10}(X_O^{met} X_{Si}^{met})$ features an approximately linear dependence on $1/T$ and, moreover, lies extremely close to the experimentally determined K_D^{Si} proposed by ref. 9, which they found to have no resolvable pressure dependence. In contrast to Si, O solubility does show a weak pressure dependence (Extended Data Fig. 3). If the mutual Si and O solubility is treated in a more thermodynamically rigorous way by relating K_{Si-O} to $X_{Si} X_O^2$, the data now fall uniformly below the modelled K_D^{Si} line, showing a dependence on O as would be expected for a mixture of O and Si in the metal.

To quantify the mutual Si and O dependence, we use K_D^O and K_D^{Si} definitions[9]

$$K_D^{Si} = \frac{X_{Si}^{met}}{X_{SiO_2}^{sil}} \times \frac{(X_{FeO}^{sil})^2}{(X_{Fe}^{met})^2}$$
$$K_D^O = \frac{X_{Fe}^{met} X_O^{met}}{X_{FeO}^{sil}} \tag{3}$$

that allows one to express $X_{Si}^{met}(X_O^{met})^2$ in terms of the K_D values and eliminate any dependence on X_{FeO}^{sil}. In particular

$$(K_D^O)^2 K_D^{Si} = \frac{X_{Si}^{met}(X_O^{met})^2}{X_{SiO_2}^{sil}} \tag{4}$$

K_D^O is weakly dependent on pressure[9], so we first correct for this by finding the best-fitting parameterization. Following previous workers[9,35–37], we fit the temperature and pressure dependence to a form

$$\log_{10}(K_D^O) = a + \frac{b}{T} + c\frac{P}{T} \tag{5}$$

with T in kelvin and P in gigapascals, and using the formula of ref. 9 for K_D^{Si}. The result is $a = 0.3009 \pm 0.1120$ and $c = -36.8332 \pm 5.5957$, showing the dominant correction to be for pressure with a slight baseline shift, which is implied by the dependence in the raw data seen in Extended Data Fig. 3. We next account for the non-ideality in the liquid metal due to Si–O interactions. Introducing activities $a_i = \gamma_i X_i$ for $i = $(Si, O) in equation (4) via

$$(K_D^O)^2 K_D^{Si} = \frac{\gamma_{Si}^{met}(\gamma_O^{met})^2}{\gamma_{SiO_2}^{sil}} \times \frac{X_{Si}^{met}(X_O^{met})^2}{X_{SiO_2}^{sil}} \tag{6}$$

we can fit the activity coefficients using the ε model[9,38] in the metal and assume $a_{ox}^{sil} = X_{ox}^{sil}$ for oxide 'ox' in the silicate. Owing to the requirement that $\varepsilon_i^j = \varepsilon_j^i$ (ref. 39), we fit at $T = T_{ref} = 1,873$ K and account for the temperature dependence of γ_i as recommended in that source: $\log\gamma_i(T) = (T_{ref}/T)\log\gamma_i(T_{ref})$. Extended Data Fig. 3 shows the fitting results, and Extended Data Table 1 lists all of the fitted values. We find, as before, that Si self-interaction in the metal is not resolvable in the data.

We calculate the solubility of SiO_2 in the top of the outer core by finding where the activity of $SiO_2 = 1$, where $a_{SiO_2}^{sil}$ is

$$a_{SiO_2}^{sil} = \frac{(X_O^{met})^2 X_{Si} \times (\gamma_O^{met})^2 \gamma_{Si}^{met}}{K_D^{Si}(K_D^O)^2} \tag{7}$$

The results are shown in Extended Data Fig. 4. The general trend is for increasing solubility with temperature, and for decreasing solubility with pressure. The model

is not fitted using any data with $P < 16$ GPa, and so makes no claims to be valid at pressures lower than this.

Buoyancy estimate. We calculated the volume of the liquid ternary Fe–Si–O alloy, $Fe_{116}Si_4O_8$ (corresponding to 3.6 wt% SiO_2), and aggregate of liquid iron and solid SiO_2 by first-principles molecular dynamics using pseudopotentials within the density-functional theory. The Perdew–Burke–Ernzerhof-type functional was used for the exchange-correlation potential[40]. The pseudopotentials for iron, silicon and oxygen atoms were generated using Vanderbilt's method[41]. The electronic configurations were $3s^23p^63d^{6.5}4s^14p^0$ for iron, $3s^23p^23d^0$ for silicon, and $2s^22p^4$ for oxygen. The cutoff radii were 1.8, 1.6 and 1.4 atomic units (1 atomic unit is 0.529177 Å) for iron, silicon and oxygen, respectively. The cutoff energy for the plane-wave expansion was 30 Ry. All calculations were carried out using the Quantum-ESPRESSO package (http://www.quantum-espresso.org)[42], with a modification to use the Nosé–Hoover thermostat[43].

For $Fe_{116}Si_4O_8$, we used a fixed cubic cell with volume of 923.116 Å^3. We performed a first-principles molecular dynamics calculation at 10,000 K for 2 ps to obtain the liquid state. Then the cell was quenched to 6,000 K and allowed to equilibrate for 2 ps. Finally, a first-principles molecular dynamics simulation was performed for 10 ps to calculate pressure by taking their averages over time. The temperature was controlled using a Nosé–Hoover thermostat[44,45]. Time steps were 2 fs at 10,000 K for generating the liquid structure, and 1 fs at 6,000 K. Thermal excitation of electrons was taken into account by the Fermi–Dirac distribution. Γ point sampling was used. The calculated pressure is 268 GPa.

At 268 GPa, a stable form of solid SiO_2 is the pyrite-type structure[46]. At this pressure, 6,000 K is close to its melting temperature[47]. Hence the quasi-harmonic approximation approach used frequently for a solid state is not appropriate for this case. Instead, first-principles molecular dynamics calculations were performed also for pyrite SiO_2. We used a cubic cell with 96 atoms, corresponding to a $2 \times 2 \times 2$ supercell of pyrite: 8×4 SiO_2. At six volumes between about 200 GPa and about 300 GPa, we performed first-principles molecular dynamics calculations from the initial atomic geometry of the pyrite structure. For all six volumes, we obtained solid states at 6,000 K after 10-ps molecular dynamics runs, confirmed by the mean squared displacements and radial distribution functions. Then pressures calculated at the six volumes were fitted to the third-order Birch–Murnaghan equation of state. Then we obtained the volume of pyrite SiO_2 at 268 GPa and 6,000 K to be 15.906 Å^3 per SiO_2. The volume of pure iron liquid at 268 GPa and 6,000 K is 7.386 Å^3 per Fe atom, based on the equation of state reported in ref. 48. A mixture of 116 atoms of pure liquid iron and solid pyrite SiO_2 with four formula units is $7.386 \times 116 + 15.906 \times 4 = 920.417$ Å^3 per $Fe_{116}(SiO_2)_4$, which is slightly smaller than but quite similar to that of liquid $Fe_{116}Si_4O_8$.

We made a similar calculation with a thermodynamic calculation of the melting relations of stishovite and of pure iron at 135 GPa and 4,000 K, and a thermodynamic model of the Fe–Si–O system for mixing properties in the liquid metal alloy. At those conditions, $\rho(Fe + 1\,wt\%\,SiO_2) = 12,746$ kg m^{-3}, and $\rho(Fe) = 12,890$ kg m^{-3}, which is a change of about 1%, very similar to the first-principles results shown above. From this the compositional expansivity is $\alpha_c = -(1/\rho) \times (\partial\rho/\partial c) = 1.117$. To calculate the crystallization yield, we used the three accretion compositions (in other words, the proposed original core compositions) shown in Fig. 2. The yields for compositions 'S', 'F' and 'R' are 2.3 wt%, 2.1 wt% and 4.5 wt% for temperature changes of 489 K, 770 K and 1,185 K, leading to an average temperature change of 0.0041 wt% SiO_2 K^{-1} or a precipitation rate of 4×10^{-5} K^{-1}. These are the input parameters for the core cooling model (see below).

Core cooling rate with SiO_2 crystallization required for a pre-inner core dynamo. Before the onset of inner-core crystallization, we consider a fully liquid core losing heat to the mantle at a total rate Q_{CMB}. The energy balance is $Q_{CMB} = Q_c + Q_L + E_{SiO_2}$ with Q_c the sensible heat (secular cooling), Q_L the latent heat of SiO_2 crystallization and E_{SiO_2} the compositional energy due to the mixing of the dense alloy released at the top of the core by the crystallization of SiO_2.

Q_c can be related to the rate of change of the CMB temperature[19] as $Q_c = -P_c \frac{dT_{CMB}}{dt}$ with $P_c = 0.054$ TW Gyr K^{-1}. The latent heat release is also tied to the cooling rate as $Q_L = -LM_{core}\frac{d\xi}{dT}\frac{dT_{CMB}}{dt}$ with latent heat $L = 4.3$ MJ kg^{-1} of SiO_2 crystallized and $d\xi/dt = 4 \times 10^{-5}$ K^{-1} (see above) the rate of change of the SiO_2 mass fraction ξ in the core as a function of temperature. Finally, the compositional energy can be computed similarly to what is usually done for the effect of light elements released at the inner-core boundary as

$$E_{SiO_2} = -\int_{V_{core}} \rho\mu''_{SiO_2}\,dV\frac{d\xi}{dT}\frac{dT_{CMB}}{dt} \qquad (8)$$

with μ''_{SiO_2} the difference in chemical potential between the average value at any depth in the core and the CMB value. Note that since Si and O change only because

of their common extraction process at the CMB and can be assumed to mix well into the core, they do not need to be treated as separate species in these equations, their respective contributions being always added as an effective SiO_2 light 'element'. Using the same core structure model as ref. 19, we obtain

$$\mu''_{SiO_2}(r) = \frac{2\pi}{3}G\rho_0\alpha_c\left(r_{CMB}^2 - r^2\right)\left(1 - \frac{3}{10}\frac{r^2 + r_{CMB}^2}{L_\rho^2}\right) \qquad (9)$$

with G the gravitational constant, $\rho_0 = 12,451$ kg m^{-3} the density at the centre of the liquid core[19], $\alpha_c = -\left(\frac{\partial\rho}{\partial\xi}\right)/\rho = 1.117$ the chemical expansion coefficient, and $L_\rho = 8,039$ km the characteristic for the density variation with radius. The compositional energy is then also proportional to the cooling rate of the CMB, $E_{SiO_2} = -P_{SiO_2}\frac{dT_{CMB}}{dt}$ with $P_{SiO_2} = 0.022$ TW Gyr K^{-1}.

The entropy balance of the fully liquid core is also written and, combined with the energy balance, provides an efficiency equation

$$\phi + T_\phi\int_{V_{core}} k\left(\frac{\nabla T}{T}\right)^2 dV = -\frac{T_\phi}{T_{CMB}}\left[\left(1 - \frac{T_{CMB}}{T_c}\right)P_c + P_{SiO_2}\right]\frac{\partial T_{CMB}}{\partial t} \qquad (10)$$

into which the latent heat does not enter since it is produced at the temperature of the CMB, which is also the temperature at which heat is removed from the core, which results in a null efficiency for that term. It does, however, contribute to the CMB heat flow. $T_\phi = 4,784$ K and $T_c = 4,795$ K are the temperatures at which dissipation ϕ and sensible heat occur on average and can be estimated (T_ϕ) and precisely computed (T_c) for a given CMB temperature, here 4,109 K at the time of the inner-core nucleation (ref. 19). Equation (10) is used to compute the cooling rate necessary to sustain a given total dissipation ϕ (Fig. 3). The dissipation due to conduction along the isentropic profile has been expressed before for the depth-dependent thermal conductivity considered here[19] and is equal to 538 MJ K^{-1}, corresponding to 2.58 TW with the value of T_ϕ estimated here. This is also converted to a rate of change of SiO_2 concentration and CMB heat flow. In the absence of SiO_2 crystallization, both latent and compositional energy are absent and the ratio between the cooling rate and the CMB heat flow are different, hence the separate scales in Fig. 3. For a total dissipation less than about 4 TW, the core dynamo can run with a CMB heat flow lower than what is conducted down the isentropic gradient (solid blue line on Fig. 3), which is about 13.5 TW with the high value for conductivity considered here[10], if the compositional buoyancy is provided by crystallizing SiO_2 at the CMB. Without that buoyancy source, the heat flow at the CMB must exceed the isentropic value (dashed green line on Fig. 3).

Data availability. All data used or analysed during this study are available from K.H. upon request.

31. Akahama, Y. & Kawamura, H. Pressure calibration of diamond anvil Raman gauge to 310 GPa. *J. Appl. Phys.* **100**, 043516 (2006).
32. Andrault, D. *et al.* Thermal pressure in the laser-heated diamond-anvil cell: an X-ray diffraction study. *Eur. J. Mineral.* **10**, 931–940 (1998).
33. Ichikawa, H., Tsuchiya, T. & Tange, Y. The P-V-T equation of state and thermodynamic properties of liquid iron. *J. Geophys. Res. Solid Earth* **119**, 240–252 (2014).
34. Morard, G. *et al.* Melting of Fe–Ni–Si and Fe–Ni–S alloys at megabar pressures: implications for the core–mantle boundary temperature. *Phys. Chem. Miner.* **38**, 767–776 (2011).
35. O'Neill, H. S. C., Canil, D. & Rubie, D. C. Oxide-metal equilibria at 2500°C and 25 GPa: implications for core formation and the light component in the Earth's core. *J. Geophys. Res. Solid Earth* **103**, 12239–12260 (1998).
36. Wade, J. & Wood, B. J. Core formation and the oxidation state of the Earth. *Earth Planet. Sci. Lett.* **236**, 78–95 (2005).
37. Tsuno, K., Frost, D. J. & Rubie, D. C. Simultaneous partitioning of silicon and oxygen into the Earth's core during early Earth differentiation. *Geophys. Res. Lett.* **40**, 66–71 (2013).
38. Ma, Z. Thermodynamic description for concentrated metallic solutions using interaction parameters. *Metall. Mater. Trans. B* **32**, 87–103 (2001).
39. Japan Society for the Promotion of Science and the Nineteenth Committee on Steelmaking *Steelmaking Data Sourcebook* Part II (Gordon and Breach, 1988).
40. Perdew, J. P., Burke, K. & Ernzerhof, M. Generalized gradient approximation made simple. *Phys. Rev. Lett.* **77**, 3865–3868 (1996).
41. Vanderbilt, D. Soft self-consistent pseudopotentials in a generalized eigenvalue formalism. *Phys. Rev. B* **41**, R7892–R7895 (1990).
42. Giannozzi, P. *et al.* Quantum ESPRESSO: a modular and open-source software project for quantum simulations of materials. *J. Phys. Condens. Matter* **21**, 395502 (2009).
43. Sun, T., Zhang, D. B. & Wentzcovitch, R. M. Dynamic stabilization of cubic CaSiO3 perovskite at high temperatures and pressures from *ab initio* molecular dynamics. *Phys. Rev. B* **89**, 094109 (2014).

44. Nosé, S. A unified formulation of the constant temperature molecular dynamics methods. *J. Chem. Phys.* **81,** 511–519 (1984).
45. Hoover, W. G. Canonical dynamics: equilibrium phase-space distributions. *Phys. Rev. A* **31,** 1695–1697 (1985).
46. Kuwayama, Y., Hirose, K., Sata, N. & Ohishi, Y. The pyrite-type high-pressure form of silica. *Science* **309,** 923–925 (2005).
47. González-Cataldo, F., Davis, S. & Gutiérrez, G. Melting curve of SiO_2 at multimegabar pressures: implications for gas giants and super-Earths. *Sci. Rep.* **6,** 26537 (2016).
48. Umemoto, K. *et al.* Liquid iron-sulfur alloys at outer core conditions by first-principles calculations. *Geophys. Res. Lett.* **41,** 6712–6717 (2014).
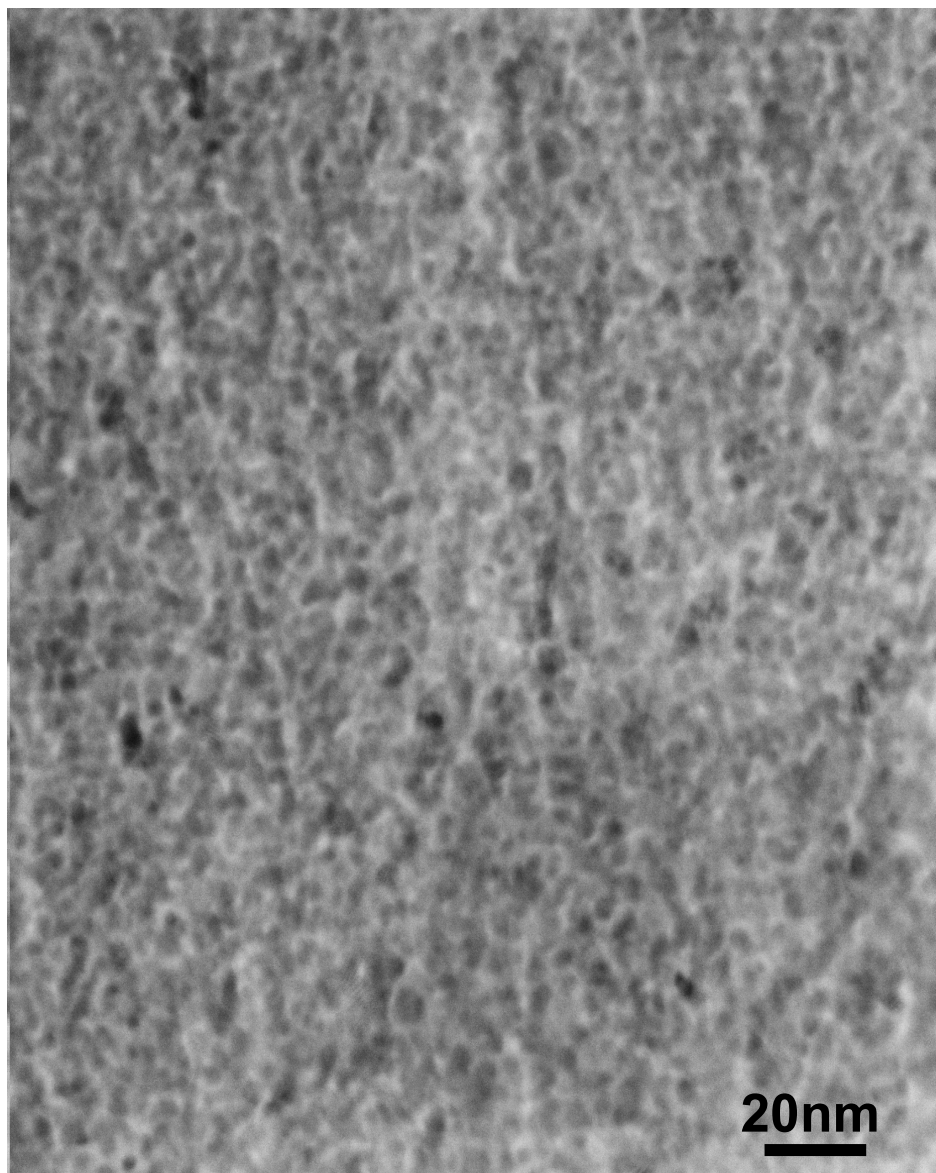
Extended Data Figure 1 | TEM bright-field image of the Fe–Si–O starting material. It consists of fine-grained (<5 nm) metal and oxide.
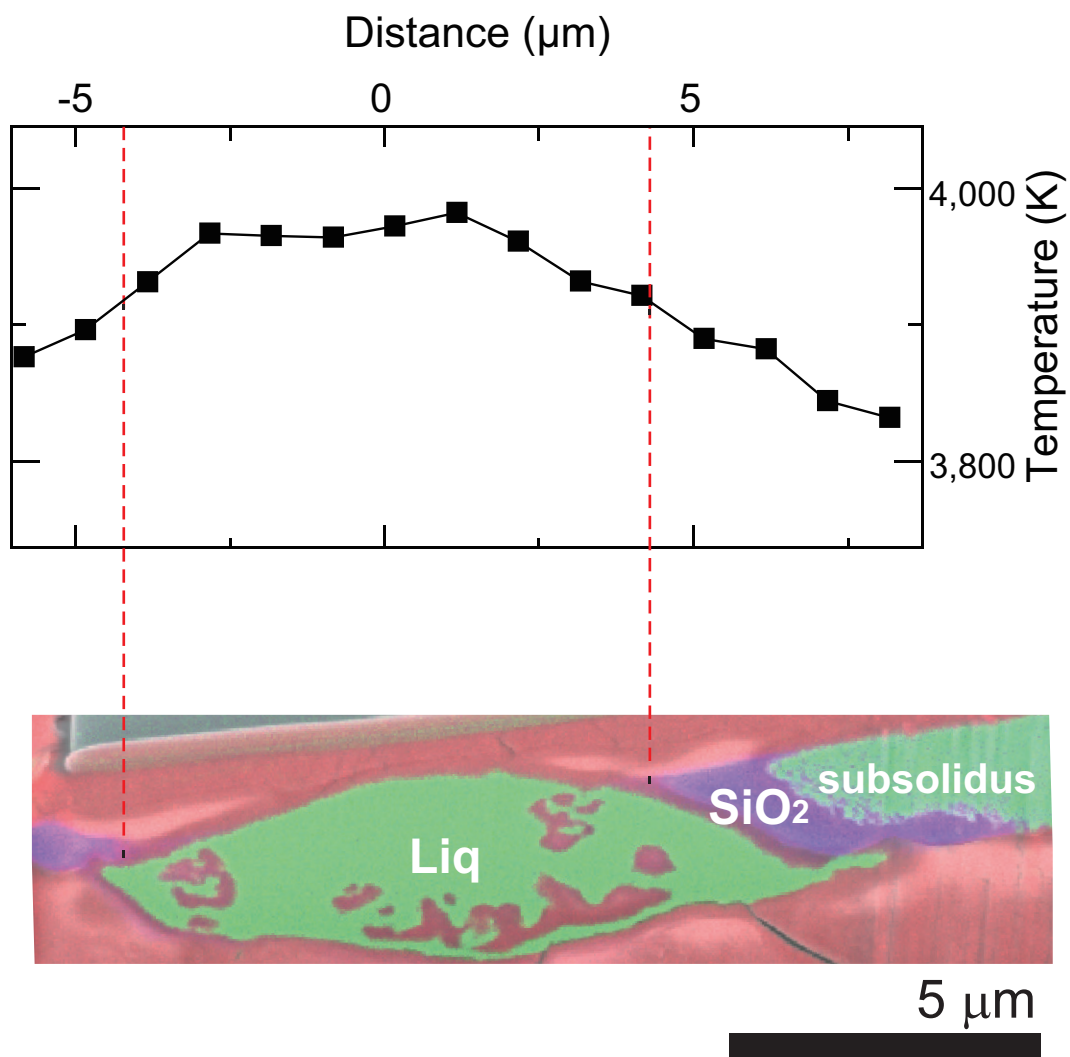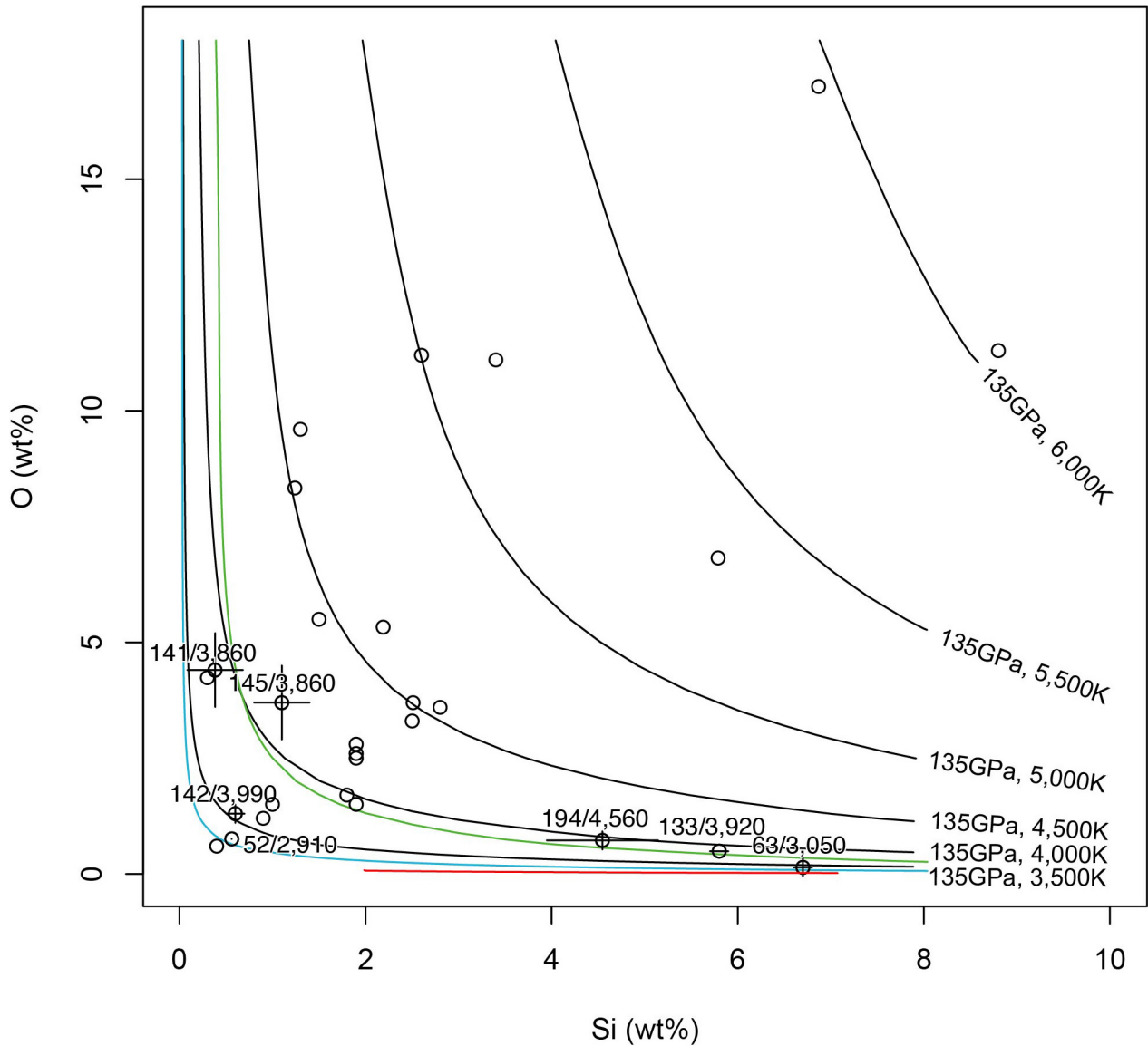
Extended Data Figure 2 | Melting experiment at 133 GPa in run 4. Radial temperature distribution (as a function of distance from the centre of the laser-heated hot spot) and the composite X-ray maps for Fe, Si, O and Al for a cross-section of the recovered sample; quenched liquid Fe–5.8 wt% Si–0.5 wt% O (green) at the centre, surrounded by solid SiO$_2$ (purple) and unmelted portion (green). They were sandwiched by Al$_2$O$_3$ insulation layers (red). Note that the central part included Al$_2$O$_3$ blocks, which is the evidence that it was molten at high pressure and high temperature.
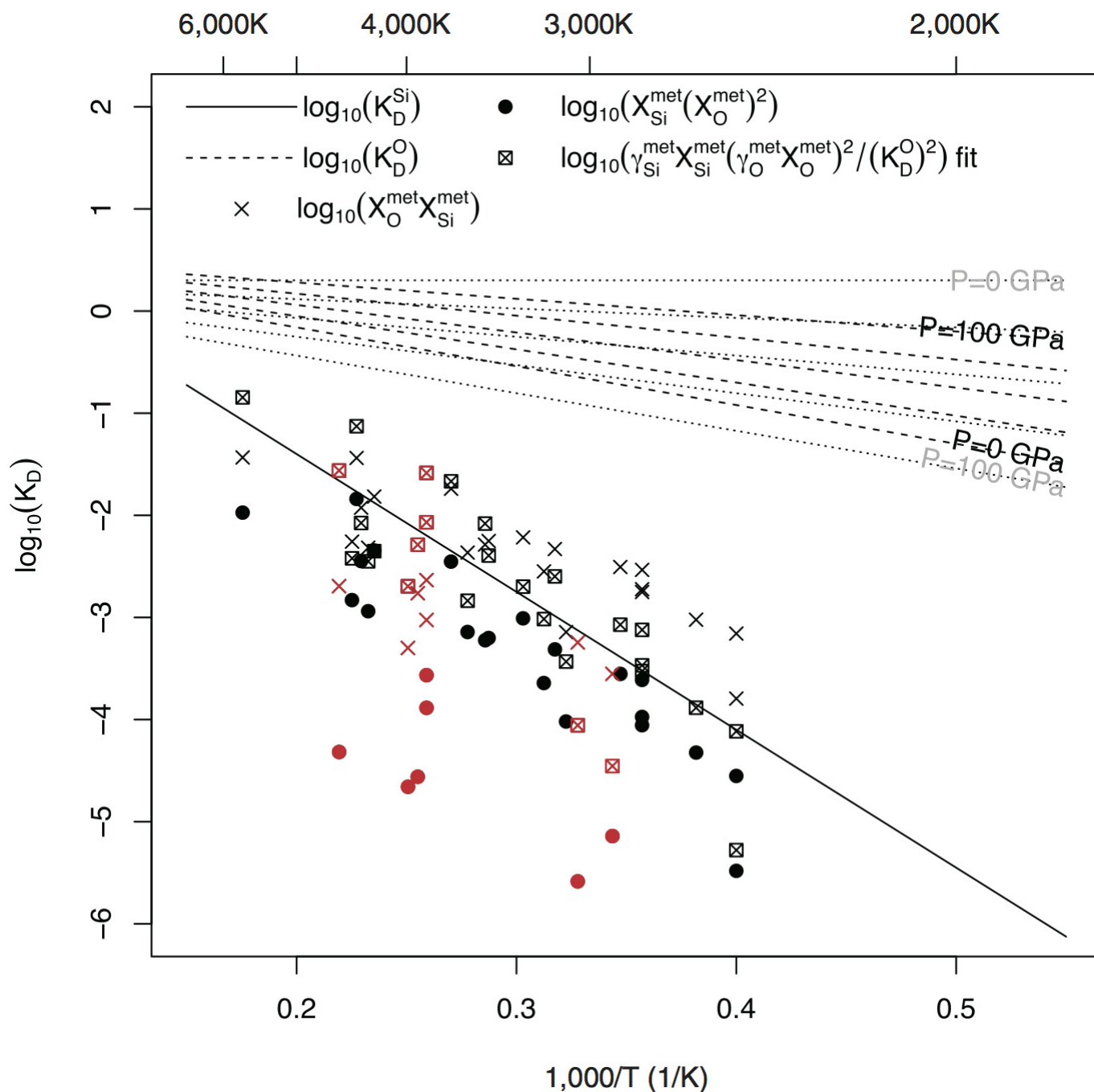
Extended Data Figure 3 | Solubility of O and Si in liquid Fe. Solid and dashed lines represent K_D^{Si} and K_D^O as parameterized by ref. 9. Points represent experimental data analysed here plotted in various ways; those in red are from this study's experiments. $\log_{10}(X_O^{met}X_{Si}^{met})$ shows an essentially linear $1/T$ dependence, similar to that found in ref. 35. More thermodynamically correct representation of the solubility K is shown by the $\log_{10}(X_{Si}^{met}(X_O^{met})^2)$ dependence, whose points spread below the K_D^{Si} line.

This suggests that X_{Si}^{met} is largely controlled by K_D^{Si}, but with additional, minor dependence on X_O^{met}. When these are accounted for by the modelling procedure described in the text, the result—an effective K_D^{Si} corrected for pressure and non-ideal Si and O interactions in the metal—is shown as $\log_{10}(\gamma_{Si}^{met}X_{Si}^{met}(\gamma_O^{met}X_O^{met})^2/(K_D^O)^2)$. Grey dotted lines show our model's K_D^O, for comparison.

Extended Data Figure 4 | Solubility limits for SiO$_2$ in liquid Fe superimposed on the present experimental results and earlier metal–silicate partitioning data. Labelled points show experimental data obtained in this study. Unlabelled points are values used in the model fits[5,7,9]. No data at pressures <16 GPa are used in the fit, so values below this limit are not well represented by the model. Black curves indicate temperature contours of SiO$_2$ saturation at 135 GPa. Green, blue and red curves are for 2,500 K at 20 GPa, 60 GPa and 100 GPa, respectively.
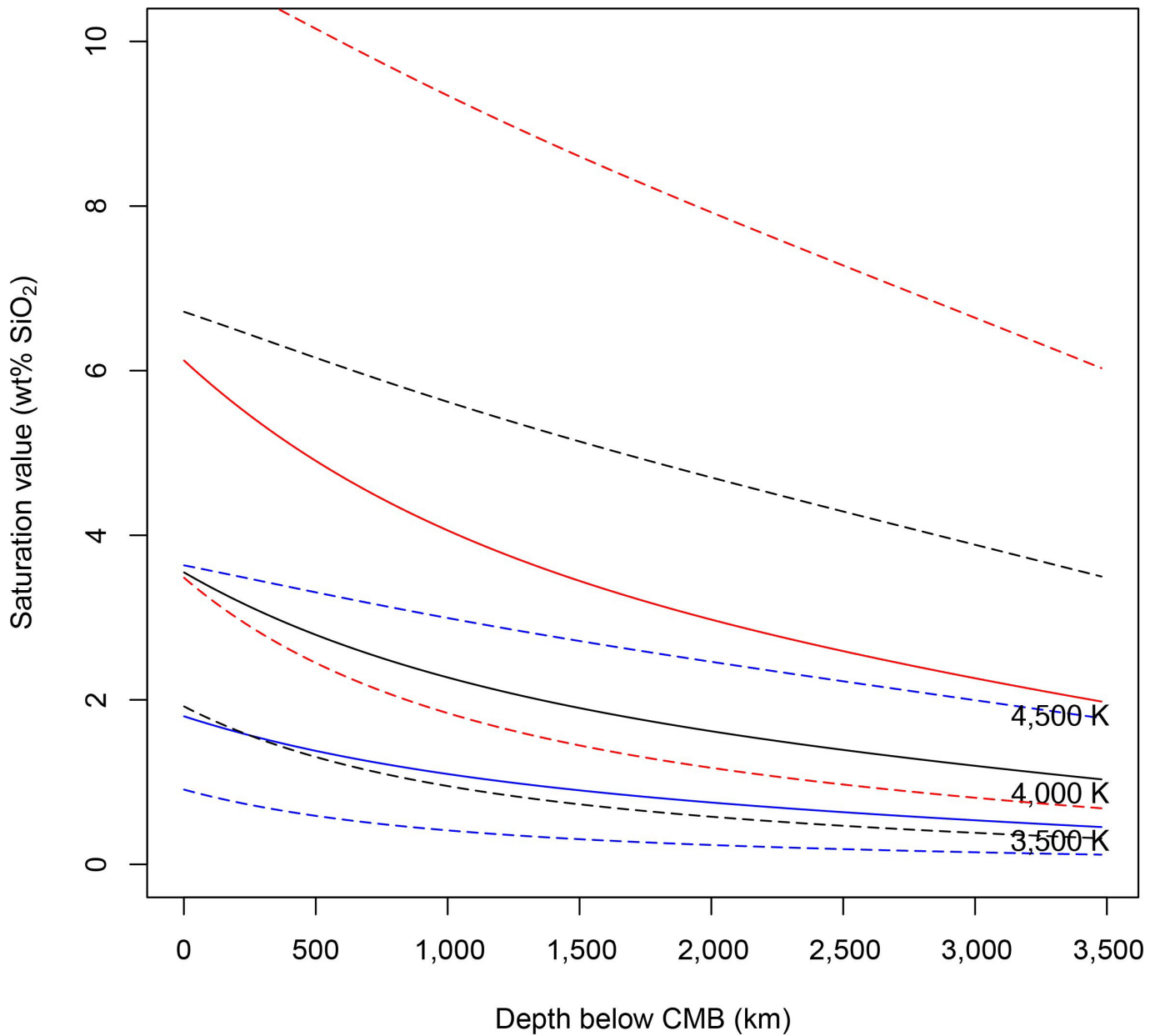
Extended Data Figure 5 | Pressure dependence of SiO₂ solubility.
For adiabats initiated at the CMB for a range of present-day core temperatures $3{,}500\,\mathrm{K} \leq T_{\mathrm{CMB}} \leq 4{,}500\,\mathrm{K}$, we show the combined pressure and temperature dependence of the solubility assuming saturation at the CMB. Each labelled solid line is bounded by the $\pm 2\sigma$ confidence interval, showing that within uncertainty, solubility is constant with depth in the core. SiO₂ crystallization at the top of the core is a likely scenario, because otherwise crystallization creates compositional stratification, which is inconsistent with seismological observations.

Extended Data Table 1 | Model parameters

	a	σ_a	b	σ_b	c	σ_c	Source
			K		K/GPa		
K_D^{Si}	1.3	0.3	-13,500	900			ref. 9
K_D^{O}	0.6	0.4	-3,800	900	22	14	ref. 9
K_D^{O}	0.30	0.11			-36.83	5.60	this study

species i	O	$\sigma_{\varepsilon_j^O}$	Si	$\sigma_{\varepsilon_j^{Si}}$			Source
ε_O^i	-7.22	1.93	-6.5	1.8			ref. 9
ε_{Si}^i	-6.5	1.8					ref. 9
ε_O^i	-9.16	4.27	7.73	4.53			this study
ε_{Si}^i	7.73	4.53					this study

a, b and c are estimated parameter values for the model $\log\left(K_D^i\right) = a + b/T + cP/T$, with formal fit uncertainties σ. ε_j^i are estimated parameter values and formal uncertainties σ for the ε model of activity coefficients in dilute iron alloys for species i and j (Si or O; ref. 38), which include the self-interaction coefficients ε_{Si}^{Si} and ε_O^O, and the mutual interaction coefficients $\varepsilon_{Si}^O = \varepsilon_O^{Si}$. Ref. 9 is a previous estimate.